

Magnetic augmentation through multi-gradient coupling enables direct and programmable profiling of circulating biomarkers

Received: 16 April 2024

Accepted: 19 September 2024

Published online: 27 September 2024

 Check for updates

Yuan Chen^{1,2,14}, Li Zhang^{1,2,14}, Xingjie Wu¹, Xuecheng Sun¹, Noah R. Sundah^{1,2}, Chi Yan Wong^{1,3}, Auginia Natalia^{1,2}, John K. C. Tam⁴, Darren Wan-Teck Lim^{5,6,7}, Balram Chowbay^{7,8,9}, Beng Ti Ang^{10,11}, Carol Tang^{10,11,12}, Tze Ping Loh^{1,13} & Huilin Shao^{1,2,4,6} ✉

Conventional magnetic biosensing technologies have reduced analytical capacity for magnetic field dimensionality and require extensive sample processing. To address these challenges, we spatially engineer 3D magnetic response gradients for direct and programmable molecular detection in native biofluids. Named **magnetic augmentation through triple-gradient coupling for high-performance detection (MATCH)**, the technology comprises gradient-distributed magnetic nanoparticles encapsulated within responsive hydrogel pillars and suspended above a magnetic sensor array. This configuration enables multi-gradient matching to achieve optimal magnetic activation, response and transduction, respectively. Through focused activation by target biomarkers, the platform preferentially releases sensor-proximal nanoparticles, generating response gradients that complement the sensor's intrinsic detection capability. By implementing an upstream module that recognizes different biomarkers and releases universal activation molecules, the technology achieves programmable detection of various circulating biomarkers in native plasma. It bypasses conventional magnetic labeling, completes in <60 minutes and achieves sensitive detection (down to 10 RNA and 1000 protein copies). We apply the MATCH to measure RNAs and proteins directly in patient plasma, achieving accurate cancer classification.

Magnetic sensor technologies measure changes in magnetic moments and offer an attractive avenue for direct and informative biomedical applications^{1,2}. Specifically, as most biological media have a low magnetic susceptibility, they appear transparent to the applied magnetic field; magnetic technologies could thus be applied for direct detection, as even crude biological specimens have negligible magnetic background³. Importantly, magnetic sensors have a remarkable capability to provide high-resolution information⁴. Their graded response,

especially to a spatially inhomogeneous 3D magnetic field, can be used to encode and decode rich information (e.g., spatiotemporal changes via magnetic resonance imaging^{5,6}). Nevertheless, conventional magnetic biosensors commonly fail to exploit these exciting intrinsic properties. Current assays typically require specialized sample labeling with magnetic nanoparticles (MNPs) and/or have reduced perception of magnetic field dimensionality^{7,8}. For example, sandwich immunosorbent assays have been established on planar giant magnetoresistive

A full list of affiliations appears at the end of the paper. ✉ e-mail: huilin.shao@nus.edu.sg

(GMR) sensors⁹. These assays not only require MNP labeling over a 2D support, but also have their detection confined to the 2D surface and magnetic response simplified as uniform over the support area. As a result, conventional magnetic biosensors entail extensive processing (e.g., need to remove strong background from unbound nanoparticles) and have reduced analytical capacity (e.g., lack sensitivity to measure small fluctuations in a complex 3D magnetic field).

To address these challenges, several advances have been made through improved magnetic sensors and assay methodologies^{10,11}. For example, magnetic sensors have been developed with enhanced materials and sensor configurations^{12,13}. Various inorganic 2D materials have been integrated with ferromagnets to establish sophisticated spintronic devices^{14,15}. These developments exploit advances in materials science and physics to enhance the sensors' functionality and performance; improved sensing of magnetic field dimensionality could be implemented and breakthrough sensitivity achieved, especially by operating the delicate devices under low temperature conditions. On the other hand, advanced magnetic assays have been developed^{16,17}. For example, more potent MNPs have been applied to configure magnetic aggregation assays¹⁸. In these assays, MNPs cluster in response to target biomarkers, resulting in a change in magnetic moment with respect to monodispersed nanoparticles. While the approach enables wash-free detection, it works on multivalent biomarkers and requires a priori knowledge of biomarker abundance, as exquisite ratiometric tuning of nanoparticle to biomarker abundance is needed to induce successful aggregation and a good signal-to-noise ratio. These implementations thus require specialized materials, sophisticated fabrication and/or stringent experimental conditions, and cannot be readily scaled nor robustly translated.

Motivated by their high programmability, we reason that responsive hydrogels offer unique opportunities to address many of the aforementioned challenges associated with magnetic biosensors^{19,20}. In particular, hydrogels can be readily adapted, through composition and architecture engineering, to spatially interface with both nanoscale molecules (e.g., biomarker targets^{21,22} and MNPs²³) and microscale sensors²⁴. We thus develop a hybrid analytical platform that utilizes DNA hydrogel to spatially engineer 3D magnetic response for sensitive and programmable molecular detection. Named **m**agnetic **a**ugmentation through **t**riple-**g**radient **c**oupling for **h**igh-performance detection (MATCH), the technology generates matching magnetic response gradients that complement the sensor's intrinsic capability to achieve direct and sensitive biomarker detection in native biological samples. Specifically, the platform comprises gradient-distributed MNPs encapsulated within responsive hydrogel pillars and suspended above a GMR sensor array. This architecture enables triple-matched gradient engineering for optimal magnetic activation, response and transduction, respectively. As target biomarkers are introduced in a graded fashion, they focally activate the hydrogel pillars to preferentially release sensor-proximal MNPs, thereby coordinating a 3D magnetic response that spatially complements the GMR sensor's intrinsic transduction responsiveness. To enable programmable detection of different types of circulating biomarkers (e.g., RNAs and proteins), we develop a molecular translation module upstream. The module recognizes different biomarkers and releases universal translator DNA sequences to activate gradient-matched magnetic detection. Collectively, the technology achieves sensitive and programmable analysis of diverse biomarkers (limits of detection: 10 copies for RNA and 1000 copies for protein). The workflow is direct and wash-free; it bypasses conventional sample processing and magnetic labeling and can be completed in <60 minutes at room temperature. Furthermore, to facilitate clinical translation, the MATCH platform could be preserved through lyophilization and recovered with robust performance. We finally apply the technology to directly measure

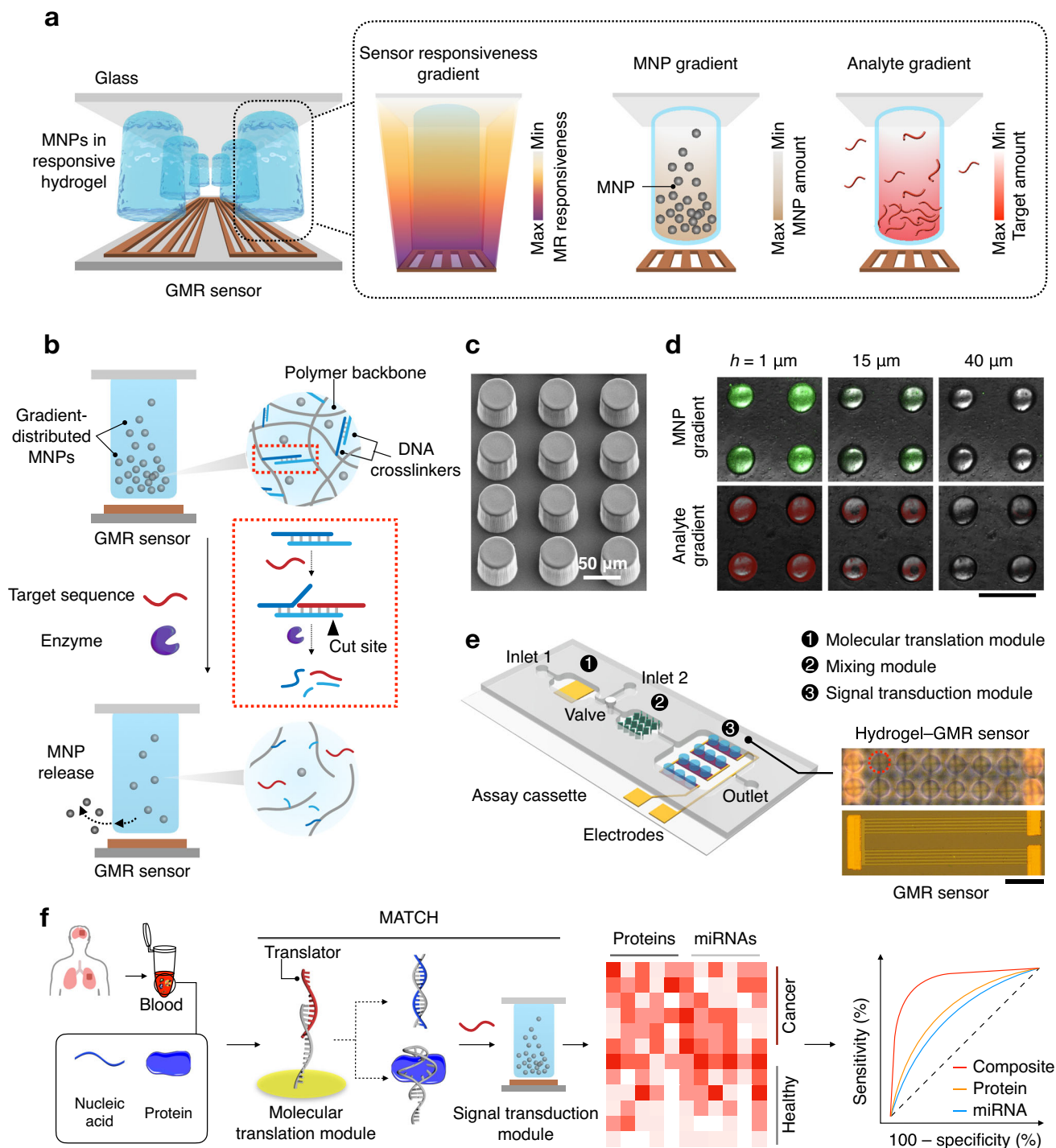
various circulating biomarkers in native patient plasma and achieve accurate cancer classification.

Results

The MATCH platform

Designed to complement the GMR sensor's intrinsic ability to detect magnetic field, the MATCH platform leverages multi-gradient engineering to enable optimal magnetic activation, response and transduction. It houses MNPs encapsulated within an array of responsive DNA hydrogel pillars suspended over a size-matched GMR sensor; the MNPs are spatially distributed to form a vertical concentration gradient within individual hydrogel pillars (Fig. 1a). This configuration thus generates an optimal 3D magnetic response by spatially matching three types of gradient profiles: an analyte distribution achieved through microfluidic tuning to focally activate, a graded MNP distribution encapsulated within responsive DNA hydrogel pillars to smartly respond, and the GMR sensor's intrinsic transduction gradient (magnetoresistive (MR) responsiveness gradient) that decays rapidly perpendicular to the sensor surface. Motivated by the sensor's intrinsic transduction responsiveness, where sensor-proximal MNPs can induce a more pronounced magnetization change in the GMR free layer and generate a larger magnetic signal than distal MNPs (Supplementary Fig. 1a), we reason that rationally designed MNP release—through focal activation by a shaped analyte distribution and preferential release of sensor-proximal MNPs in a gradient distribution—can generate a matching magnetic response that spatially complements the sensor's intrinsic capability and enhance the transduction (Supplementary Fig. 1b–c).

We thus developed the MATCH system through multi-gradient coordination. First, to establish a MNP distribution that is complementary to the MR responsiveness gradient and changes upon analyte activation, we embedded MNPs in hydrogel pillars (Fig. 1b). The responsive hydrogel system, comprising poly(sodium acrylate) chains crosslinked by two hybridizing DNA strands (Supplementary Table 1), was designed to 1) entrap and establish the MNP distribution, and 2) release the nanoparticles upon analyte activation. For MNP entrapment, MNPs were gradient-encapsulated within the hydrogel pillars, under the influence of an external magnetic field during gel curing (Supplementary Figs. 2–3). For MNP release, only on-target DNA sequences can hybridize with the hydrogel crosslinkers; this DNA hybridization forms distinct enzyme cleave sites that disrupt the hydrogel, releasing the embedded MNPs in a target-specific manner (Supplementary Fig. 4). Second, to tune the target analyte gradient, we adjusted the vertical gap spacing between the GMR sensor and the suspended hydrogel pillars to shape the analyte distribution, enriching the analyte adsorption at the interfacial gaps to focally activate the hydrogel system (Supplementary Fig. 5). Molecular characterization of the developed system confirmed not only tunable assembly of the hydrogel pillars (Fig. 1c) but also complementary establishment of the MNP gradient and analyte gradient, respectively (Fig. 1d). Leveraging multi-module microfluidics (Fig. 1e), we further developed the MATCH platform as a rapid wash-free assay for the direct and programmable detection of various target molecules (Supplementary Figs. 6–7). Specifically, the platform incorporates a molecular translation module that supports expanded detection of different types of analytes (e.g., nucleic acids and proteins) and a GMR transduction module that enables multi-gradient matching to maximize the sensor's detection capability (Supplementary Fig. 8). The molecular translation module recognizes different targets to displace a pool of translator DNA sequences; these translator strands contain a common sequence motif to activate hydrogel response and signal transduction, thereby enabling robust and multiplexed biomarker detection (Fig. 1f). Employing the MATCH platform, we measured circulating miRNA and protein biomarkers in lysed plasma samples of cancer patients and developed composite signatures to accurately distinguish the patients.



Multi-gradient matching

To develop the gradient-matched transduction platform, we first established the responsive hydrogel system to encapsulate and release MNPs (Fig. 2a). To confer molecular specificity, we incorporated DNA crosslinkers to construct the hydrogel pillars. Specifically, we mixed the hydrogel precursors, comprising sodium acrylate monomer and acrydite-modified DNA crosslinkers, with MNPs and photoinitiator. The mixture was cured under UV and assembled as suspended pillar structures above the GMR sensor (Supplementary Fig. 2). To maximize the pillar formation efficiency (Supplementary Fig. 9), we evaluated various hydrogel composition and UV curing conditions (Fig. 2b, left). For parameters that achieved >95% pillar formation efficiency, we further optimized them for responsive MNP release (Fig. 2b, right). To

induce MNP release, we incubated the nanoparticle-loaded hydrogel pillars with target DNA sequences and nicking endonuclease. The optimized pillars showed a marked increase in hydrogel porosity upon target sequence incubation and efficient MNP release for GMR signal transduction (Supplementary Fig. 10).

Employing the responsive hydrogel pillars, we next established the platform architecture for multi-gradient matching. To complement the sensor's intrinsic MR responsiveness profile, that extends and decays rapidly perpendicular to the sensor surface (Fig. 2c), we accordingly designed a matching MNP distribution and analyte distribution (i.e., target-displaced translator sequence) to preferentially release sensor-proximal MNPs for optimal signal transduction (Supplementary Fig. 1c). Specifically, to establish the MNP distribution, we

Fig. 1 | The MATCH platform. **a** Schematic of the MATCH platform. The technology leverages multi-gradient matching to engineer 3D magnetic response for direct and programmable biomolecular detection in native biofluids. It features an array of responsive DNA hydrogel pillars suspended above a GMR sensor; each pillar encapsulates gradient-distributed MNPs which are released upon target incubation. To match the sensor's intrinsic responsiveness gradient (i.e., that decays rapidly perpendicular to the sensor surface), the MNP and analyte gradients are enriched near the tips of the hydrogel pillars. Target analyte can focally activate the hydrogel pillars to preferentially release sensor-proximal MNPs, generating a magnetic response that spatially complements the sensor's intrinsic detection capability. **b** Target-induced MNP release from the hydrogel pillars. The MNP-embedded hydrogel pillars comprise polymer backbones and DNA crosslinkers. Target analyte hybridizes with one of the DNA crosslinkers and displaces the other, forming an endonuclease (Nb.BssSI) cut site. Enzymatic cleavage disrupts the hydrogel network and releases the encapsulated MNPs, causing a change in the GMR magnetic signal. **c** Scanning electron micrograph of the MATCH hydrogel pillar array. This experiment was repeated thrice independently with similar results.

d MNP and analyte gradients. Confocal fluorescence images at different heights of the hydrogel pillars (*h*) encapsulating ATTO590-conjugated MNPs (top) or incubated with FAM-labeled analyte (bottom) confirmed the establishment of the MNP and analyte gradients, respectively. Scale bar, 100 μm . This experiment was repeated thrice independently with similar results. **e** Schematic of the MATCH microfluidic device. To complement the MATCH assay workflow, the device integrates the following functional modules: (1) molecular translation module for target recognition and translator release; (2) mixing module, an array of 45° parallelogram barriers to improve local mixing; (3) signal transduction module with MNP-loaded hydrogel pillars for gradient-matched detection of the released translators. The inset shows optical micrographs of the GMR sensor before (top) and after (bottom) the patterning of the hydrogel pillars (red circle). Inset scale bar, 100 μm . **f** MATCH platform for cancer diagnostics. The technology combines molecular translation and gradient-matched transduction for direct, sensitive detection of circulating nucleic acid and protein biomarkers in native plasma lysates, and effectively distinguishes cancer patients from healthy individuals.

applied an external magnetic field under the sensor during hydrogel curing (Supplementary Fig. 11). Using fluorescently-labeled MNPs, we characterized the MNP encapsulation profile within the hydrogel pillars and confirmed dense MNP concentration near the pillar tips (Fig. 2d and Supplementary Fig. 3). To generate the matching analyte gradient, through numerical simulation (Supplementary Fig. 12) and experimental validation (Fig. 2e), we found that by controlling the gap spacing between the hydrogel pillar and the sensor surface (Supplementary Fig. 13), we could achieve focal adsorption of analyte molecules onto the hydrogel pillar tips. The optimized architecture, comprising gradient-distributed MNPs encapsulated within responsive hydrogel pillars suspended over a GMR sensor, thus matches both the MNP gradient and the analyte gradient, concentrating them near the sensor's surface. Employing this architecture, we investigated the MNP release kinetics from the hydrogel through magnetic and fluorescence measurements (Fig. 2f). The coupled MNP and analyte gradients enabled a fast assay response where the magnetic signal plateaued at ~20 min. We next compared the sensitivity of the triple gradient-matched system (i.e., MNP gradient and analyte gradient complementary to the MR responsiveness) with that of partially-matched and unmatched configurations (Fig. 2g). The triple-matched architecture demonstrated the best limit of detection (LOD = 10 copies), which is $>10^4$ fold more sensitive than the others.

Modular and programmable target detection

To enable programmable detection of different types of targets (e.g., nucleic acids and proteins), we next incorporated an upstream molecular translation module to convert different biomarker targets into translator DNA sequences; these translator strands bear a universal domain that activates the triple gradient-matched magnetic transduction (Fig. 3a). Specifically, the module comprises an immobilized, target-binding recognizer DNA strand and a partially-hybridized translator strand (Supplementary Fig. 14a–b). The recognizer is made complementary to its molecular target; it acts either as a linear strand that hybridizes directly to its nucleic acid target or as a 3D aptamer structure that affinity-binds to its protein target. The translator strand consists of a variable region that duplexes with the recognizer and an overhanging conserved region that is universal and complementary to the hydrogel DNA crosslinkers. As the molecular target competitively binds to the recognizer strand, it displaces the translator strand, activating enzymatic reactions downstream to release MNPs from the hydrogel pillars and induce GMR transduction.

To optimize the molecular translation module, we tuned both the variable and conserved region of the translator strand (Supplementary Table 2). To improve the targeting capability and accommodate different types of molecular targets (e.g., nucleic acids and proteins), we first tuned the variable region of the translator sequence. By varying

the length of the translator's variable region and evaluating the amount of target-displaced translator strands, we found that strong-binding targets (e.g., long RNAs and proteins with high-affinity aptamers) require a longer variable region to achieve optimal translator displacement (Fig. 3b). Weak-binding targets conversely require a shorter variable region to achieve a comparable level of translator displacement. We then tuned the conserved region of the translator to maximize its ability to induce GMR transduction (Fig. 3c). By varying the length of the translator's conserved region and measuring the amount of resultant MNPs released, we determined that a 16-nucleotide conserved region generated the best signal transduction. Importantly, when treated with equal amounts of translator sequences that bear identical conserved region but different variable sequences (i.e., as released by different molecular targets), the magnetic platform generated comparable signals (Supplementary Fig. 15). This confirms that the approach can be applied to measure diverse molecular targets and achieves consistent magnetic transduction.

We next evaluated the performance of the integrated MATCH platform comprising the molecular translation module and the gradient-matched transduction module. Collectively, the technology achieved substantial target translation in as little as 30 minutes and enabled programmable detection across multiple types of molecular targets (miRNA, mRNA and protein) (Supplementary Fig. 14c–d). Specifically, we established MATCH assays for a diverse range of target types: long mRNA (*ACTB* and *GAPDH*), short miRNA (*miR-21-5p*, *miR-16-5p* and *miR-30d-5p*), and proteins (CD63, CD24, EpCAM, MUC1 and EGFR) (Fig. 3d). We confirmed strong signals upon specific target incubation and negligible background signals with off-target incubation. Importantly, as compared to conventional magnetic assays which assume a sandwich configuration and require multiple sample processing and magnetic labeling steps (Supplementary Fig. 16a–b and Supplementary Table 3), the MATCH platform features a flow-through wash-free assay and achieves more sensitive detection (Fig. 3e). Its limits of detection (~10 copies for nucleic acid and ~1000 copies for protein) were $\sim 10^5$ - and $\sim 10^4$ -fold better than respective conventional assays (Supplementary Fig. 16c–d).

Extracellular vesicle miRNA and protein profiling

We applied the MATCH platform to measure molecular targets in crude biological samples. As the technology leverages magnetic sensing and detects through direct target binding, it benefits from the negligible magnetic background in biological specimens and enables a streamlined workflow (i.e., wash-free target translation and signal transduction) that bypasses extensive processing (Supplementary Fig. 7). These features make the technology particularly well-suited for direct detection in complex biological samples. To verify its performance, we employed the platform to first measure RNA and protein

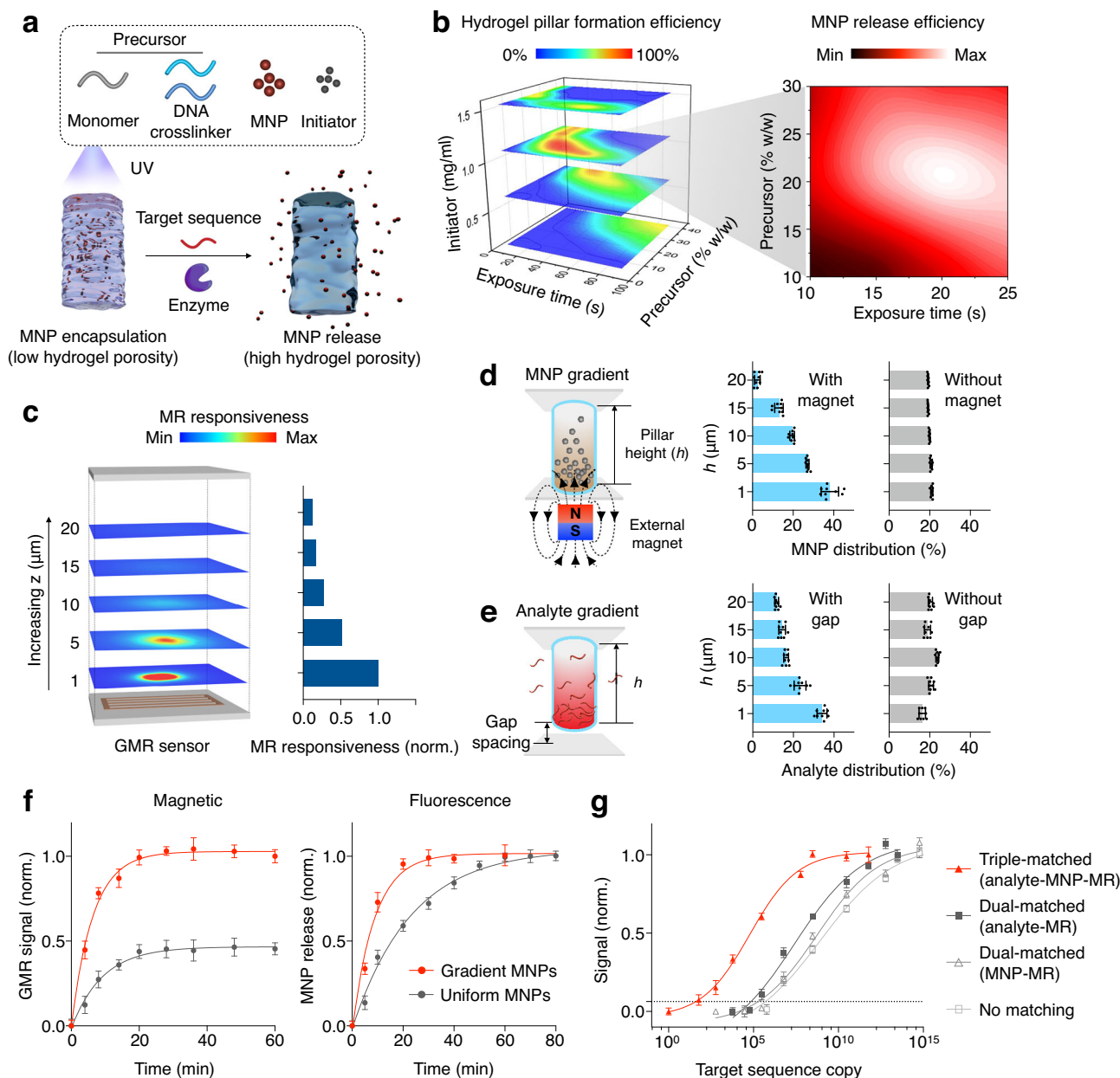


Fig. 2 | Multi-gradient engineering. **a** Responsive hydrogel system. The hydrogel pillars are formed by curing a mixture of precursor molecules (monomers and DNA crosslinkers), MNPs and initiators under UV irradiation. Upon DNA target incubation, the hydrogel network is disrupted, increasing its porosity and releasing the encapsulated MNPs. **b** Characterization of pillar formation and MNP release efficiency. We optimized various hydrogel conditions to achieve > 95% pillar formation efficiency, and further optimized these conditions for specific and efficient MNP release (right). **c** MR responsiveness gradient. Magnetized MNPs were simulated at various vertical distances (z) above the GMR sensor surface, confirming that the sensor is the most responsive at its surface. **d** MNP gradient. An external magnetic field was applied before pillar gelation to form a complementary MNP gradient. We measured the relative abundance of ATTO590-conjugated MNPs at different heights (h) of the formed hydrogel pillars and confirmed MNP enrichment near the pillar tips and the GMR sensor. **e** Analyte gradient. We adjusted the gap spacing

between the hydrogel pillars and the sensor surface to shape the analyte gradient and concentrate the analyte molecules on the pillar tips. **f** MNP release profile. By embedding ATTO590-labeled MNPs, either in gradient or uniform distribution, in the hydrogel pillars, we showed through both magnetic and fluorescence measurement that the gradient-distributed system showed a faster release kinetics. **g** Titration analysis of the triple-matched, dual-matched and unmatched assays. We compared the performance of the four architectures. The triple-matched system (analyte–MNP–MR) showed the best LOD, while the other configurations (analyte–MR, MNP–MR, no matching) showed less sensitive detection. The LOD is defined as $3 \times \text{s.d.}$ above the signal of the no-target sample. Data ($n = 9$) were collected from different pillars in **d–e**. All measurements were performed in triplicate ($n = 3$ independent experiments) and the data are displayed as mean \pm s.d. in **f–g**, and as mean in **b**. Source data are provided as a Source Data file.

targets spiked into cell lysates prepared by various chemical, thermal and mechanical lysis methods (Supplementary Fig. 17a). In all lysate conditions, the MATCH platform achieved comparable signals to that measured in a purified buffer environment. In contrast, gold standard approaches (e.g., RT-qPCR) suffered a marked signal decrease when applied to crude lysates, likely due to the undesirable effects of

enzyme inhibition and sample loss during the conventional assays' lengthy and complex processing (Supplementary Fig. 17b).

Motivated by its robust performance, we next employed the technology to measure circulating proteins and miRNAs in lysed extracellular vesicles (EVs)^{25,26}. We collected and lysed vesicles derived from human cancer cell lines of various origins: ovarian (CaOV3),

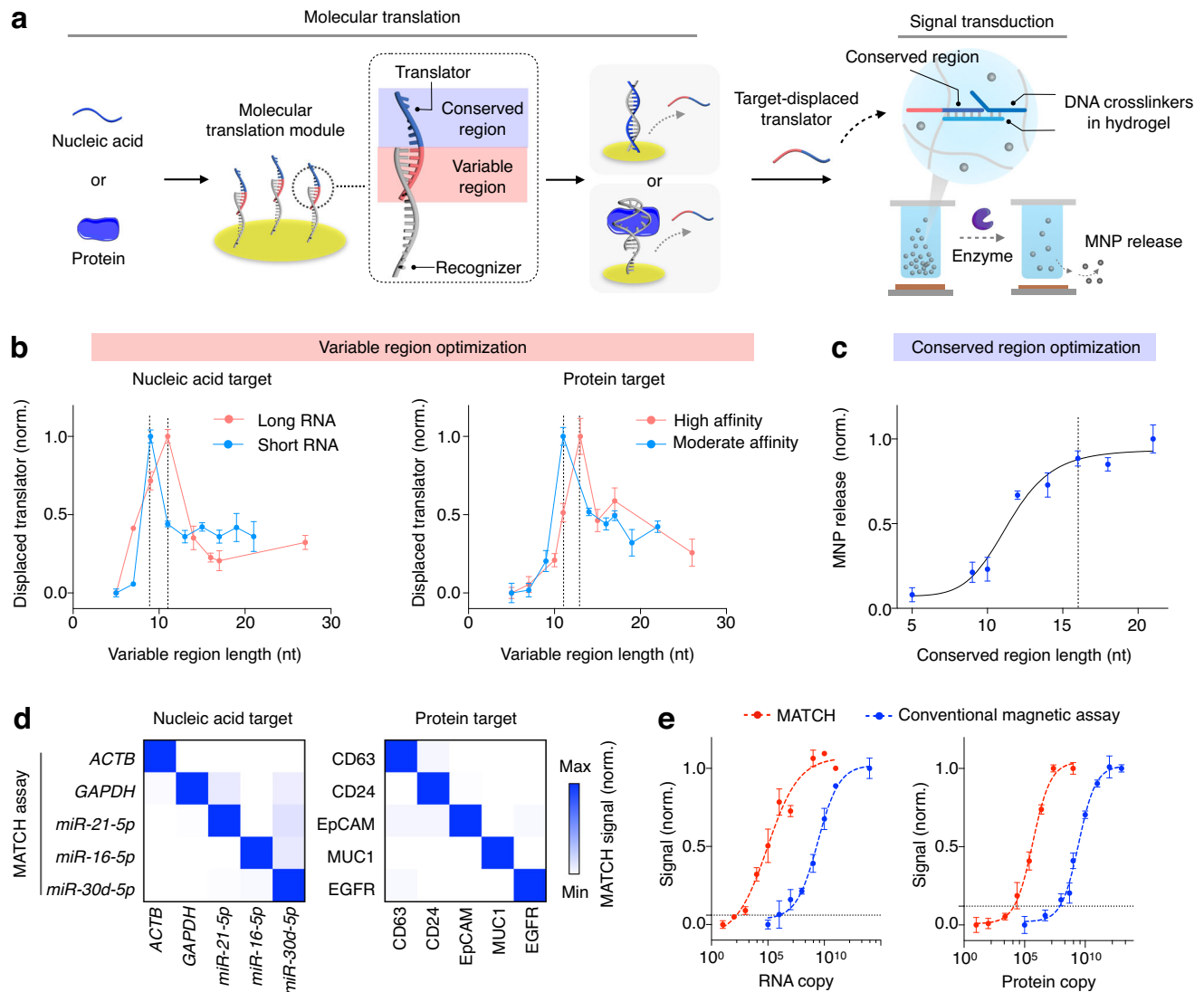


Fig. 3 | Programmable MATCH assays for profiling of different molecular targets. **a** Schematic of the MATCH molecular translation and signal transduction. The translation module comprises an immobilized, target-binding recognizer DNA strand (gray) and a partially hybridized translator strand (red). The translator strand consists of a target-specific variable region that binds the recognizer and a conserved region complementary to the hydrogel's DNA crosslinker in the signal transduction module. During molecular translation, the target (nucleic acid or protein) displaces the translator, which then hybridizes through its conserved region with the DNA hydrogel crosslinker, to form a cut site for nuclease activity. Enzymatic cleavage disrupts the hydrogel network, releases MNPs and causes a GMR signal change. **b** Optimization of the translator's variable region. Using fluorescently-labeled translators with different-sized variable regions, the molecular translation module was incubated with a fixed target concentration (10 μ M) and the displaced translators were monitored spectroscopically. For different-sized RNA targets (short, 22 nt; long, 76 nt) and protein targets with different binding affinity (high affinity, MUC1; moderate affinity, CD63), we observed that strong-

binding targets (e.g., long RNAs and proteins with high-affinity aptamers) require a longer variable region to achieve optimal translator displacement. **c** Optimization of the translator's conserved region. The length of the variable region was tuned to optimize for MNP release. Maximum MNP release was achieved when the conserved region was 16 nucleotides. **d** MATCH assay specificity. MATCH assays targeting different RNAs (*ACTB*, *GAPDH*, *miR-21-5p*, *miR-16-5p* and *miR-30d-5p*) and proteins (CD63, CD24, EpCAM, MUC1 and EGFR) were subjected to various RNA and protein molecules, respectively. All assays demonstrated specific detection. Heat map signals were assay (row)-normalized. **e** Assay sensitivity. The MATCH assays were performed on a titration of nucleic acid (*miR-21-5p*) and protein (EGFR) targets. Conventional magnetic sandwich assays were also performed as comparisons. The detection limit is defined as $3 \times$ s.d. above the signal of the no-target sample. All measurements were performed in triplicate ($n = 3$ independent experiments) and the data are displayed as mean \pm s.d. in (**b**, **c** and **e**) and as mean in (**d**). Source data are provided as a Source Data file.

gastric (MKN45 and SNU484), colorectal (HCT116 and DLD-1) and lung (H3255 and PC9). For protein profiling, we performed the MATCH measurements against a pan-EV marker (CD63)²⁷ and four putative cancer markers (CD24, EpCAM, MUC1 and EGFR)²⁸ in native vesicle lysates (Fig. 4a). As a control, we conducted comparative measurements of purified EVs using gold-standard ELISA to evaluate the protein expression profile. The MATCH measurements demonstrated a high correlation with the gold-standard ELISA ($r = 0.9293$; Fig. 4b). For miRNA profiling, we selected a panel of cancer-

associated miRNAs^{29,30}: *miR-17-5p*, *miR-21-5p*, *miR-30d-5p*, *miR-182-5p*, *miR-199a-3p*, *miR-221-3p*, *miR-222-3p*, *miR-223-3p* and *miR-486-5p*. We performed the MATCH measurements in EV lysates as well as conventional RT-qPCR analysis on purified RNA samples extracted from the same EV lysates (Fig. 4c). Likewise, the MATCH measurements demonstrated a good correlation with conventional quantification ($r = 0.7792$; Fig. 4d). Both comparative studies thereby confirmed the platform accuracy for multi-typing different biomarkers directly in complex biological samples.

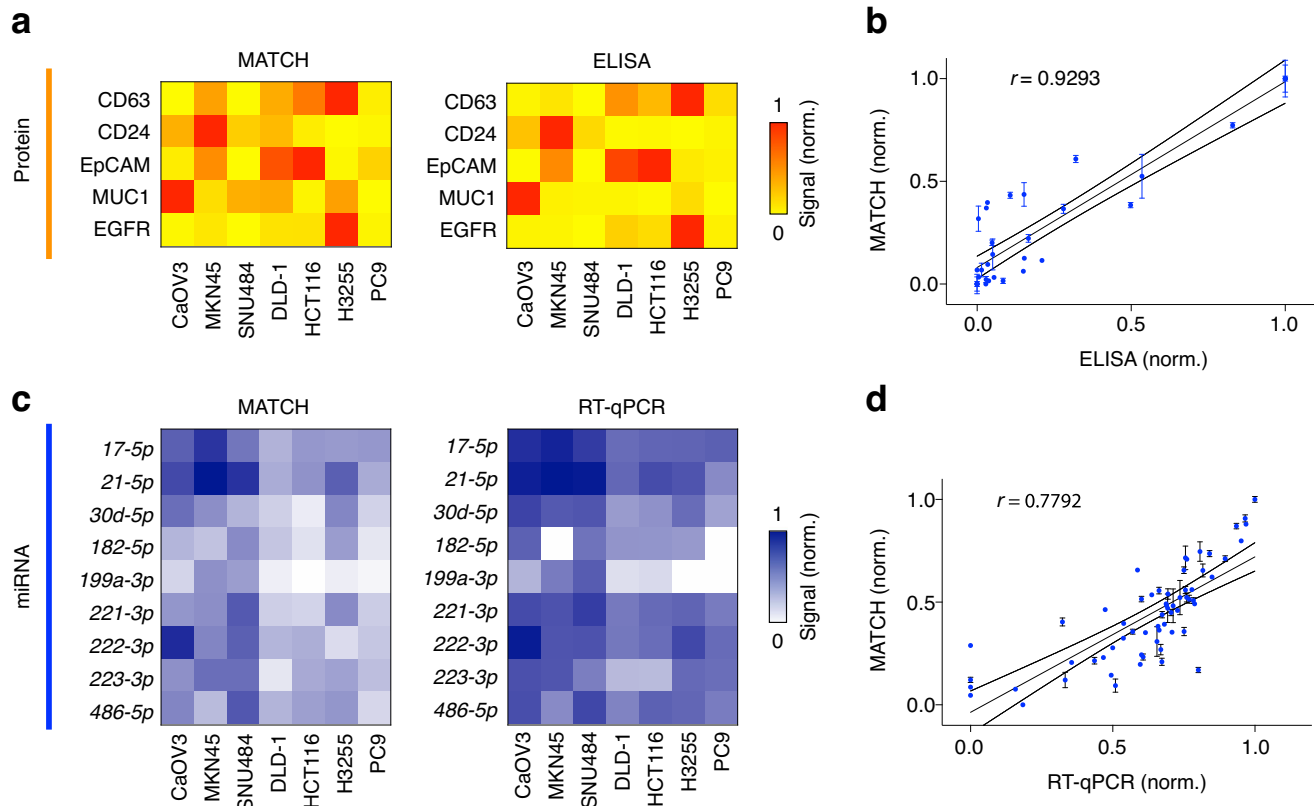


Fig. 4 | MATCH analysis of protein and miRNA markers. a Profiling of EV protein markers. MATCH was employed to profile protein markers (CD63, CD24, EpCAM, MUC1 and EGFR) in the lysates of EVs derived from various human cancer cell lines: ovarian (CaOV3), gastric (MKN45 and SNU484), colorectal (DLD-1 and HCT116) and lung (H3255 and PC9). Measurements were also performed with gold-standard ELISA as a comparison. Protein marker signals were normalized to that of GAPDH as the internal control. **b** Correlation of MATCH and ELISA. MATCH demonstrated good agreement with gold-standard ELISA measurements (Pearson's $r = 0.9293$). **c** Profiling of EV miRNA markers. MATCH was employed to profile miRNA markers (*miR-17-5p*, *miR-21-5p*, *miR-30d-5p*, *miR-182-5p*, *miR-199a-3p*, *miR-221-3p*, *miR-222-*

3p, *miR-223-3p* and *miR-486-5p*) in EV lysates derived from the same set of human cancer cell lines as in **a**. Measurements of purified RNA samples extracted from the same EV lysates were also performed with gold-standard RT-qPCR as a comparison. miRNA signals were normalized to the total RNA amounts of respective samples. **d** Correlation of MATCH and RT-qPCR. MATCH demonstrated good agreement with gold-standard RT-qPCR measurements (Pearson's $r = 0.7792$). All measurements were performed in triplicate ($n = 3$ independent experiments) and the data are displayed as mean \pm s.d. in (**b** and **d**) and as mean in **a** and **c**. Source data are provided as a Source Data file.

MATCH analysis of clinical plasma

To enhance its clinical adoption and implementation, we freeze-dried and vacuum-packed the MATCH chips to facilitate stable storage and rapid deployment (Fig. 5a). The dehydrated chips were recovered by rehydration before sample application (Supplementary Fig. 18a–b). As compared to the as-prepared without dehydration, the freeze-dried assay demonstrated robust performance. It remained stable even after three weeks of storage at room temperature and showed comparable activity and structural integrity upon rehydration recovery (Supplementary Fig. 18c–d). To evaluate the clinical utility of the MATCH platform for cancer diagnosis, we finally conducted a feasibility study using lung cancer and glioblastoma (GBM) disease models. We aimed at addressing the following key questions: (1) if the MATCH platform can be applied directly to native patient plasma samples for protein and RNA measurements, (2) the accuracy of the MATCH assays in diagnosing cancers using composite protein and RNA markers.

We obtained blood samples from lung cancer patients ($n = 26$), GBM patients ($n = 26$) and control subjects ($n = 18$), and randomized these samples into two representative cohorts (i.e., training and validation, Supplementary Table 4) to independently evaluate the robustness of the MATCH analysis on lysed plasma samples (Supplementary Fig. 19). In the training cohort that comprises 16 disease samples and 8 control samples, we measured three protein and five miRNA markers associated with each disease (Fig. 5b–c). Through

leave-one-out cross-validation, we developed regression scoring models for disease diagnosis with different combinations of biomarkers. Comparing the different analyzes, we found that the composite index score (i.e., a combination of protein and miRNA markers) could effectively distinguish the cancer and control samples (Fig. 5d–e). Other analytical models involving single marker types showed reduced performance in differentiating the clinical groups (Supplementary Fig. 20a–d). Receiver operating characteristic (ROC) curves further confirmed that the composite models achieved a high diagnostic accuracy (area under curve (AUC) = 0.9141, Fig. 5f; AUC = 0.9605, Fig. 5g). Interestingly, using biomarkers associated with both lung cancer and GBM, the MATCH technology could distinguish the two cancers (Supplementary Fig. 20e–f), indicating good potential for disease classification. To evaluate the performance of the MATCH classification, we further assessed the technology in an independent validation cohort comprising 10 lung cancer samples, 10 GBM samples and 10 control samples (Fig. 5h–i). As compared to the training cohort, the validation study showed comparable performance and achieved accurate disease classification (AUC = 0.9300, Fig. 5j; AUC = 0.9100, Fig. 5k).

Discussion

Motivated by their programmability to interface with different-sized sensing elements (e.g., nanoscale MNPs and microscale sensors), we

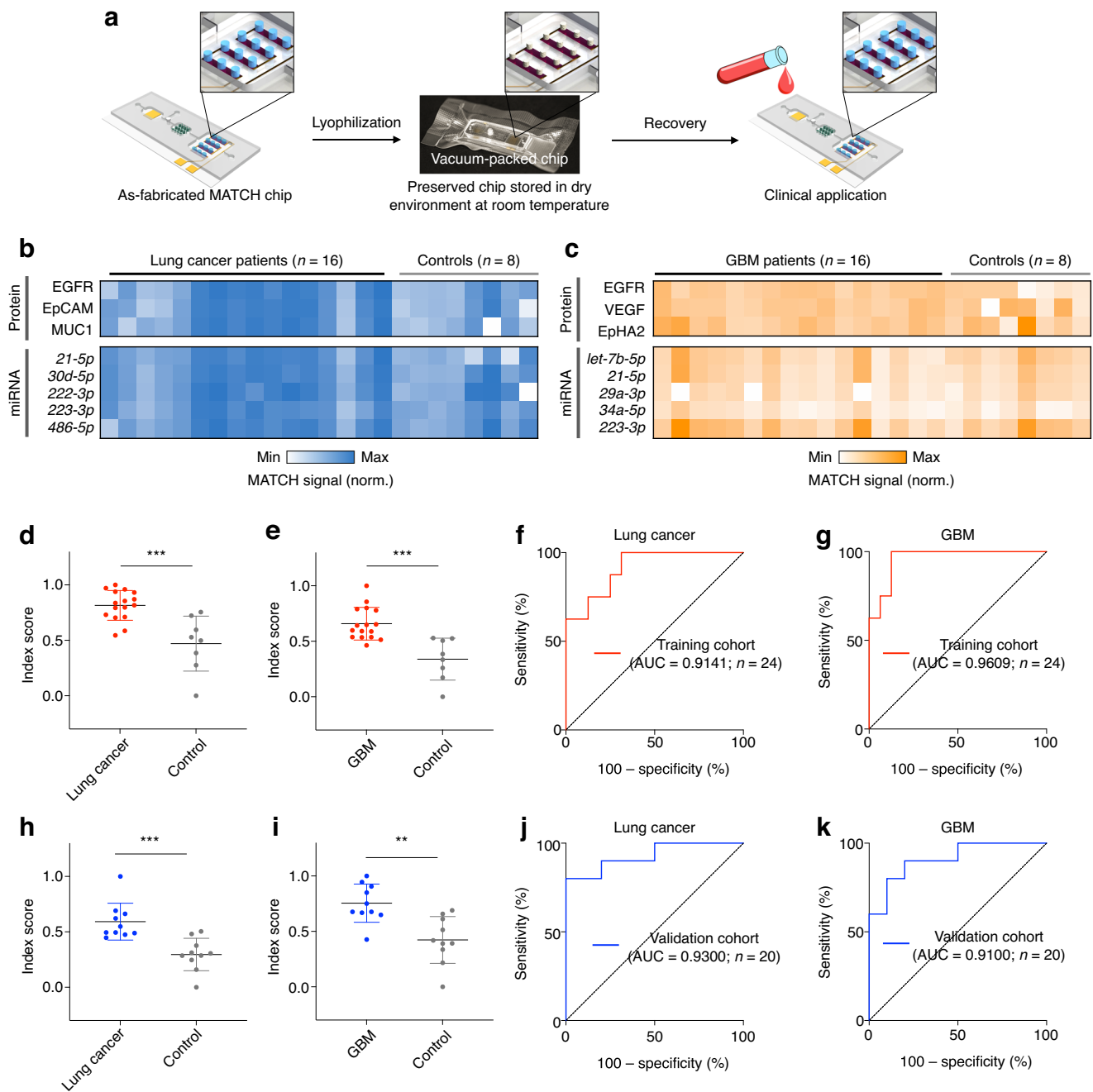


Fig. 5 | Direct profiling of clinical patient samples. **a** Storage and application. The MATCH chips, each implemented with a molecular translation module and a gradient-matched signal transduction module, were lyophilized, vacuum-packed and stored at room temperature for long-term preservation. Upon rehydration, the MATCH chips recovered with good performance. **b** MATCH measurements of lung cancer samples. Plasma samples collected from lung cancer patients ($n = 16$) and healthy controls ($n = 8$) were used as the lung cancer training cohort and profiled with the MATCH platform for three protein markers (EGFR, EpCAM and MUC1) and five miRNA markers (*miR-21-5p*, *miR-30d-5p*, *miR-222-3p*, *miR-223-3p* and *miR-486-5p*). **c** MATCH measurements of GBM samples. Plasma samples collected from GBM patients ($n = 16$) and healthy controls ($n = 8$) were used as GBM training cohort and profiled with the MATCH platform for three protein markers (EGFR, VEGF and EpHA2) and five miRNA markers (*let-7b-5p*, *miR-21-5p*, *miR-29a-3p*, *miR-34a-5p*, *miR-223-3p*). **d–e** Assessment of the training cohort ($n = 40$; 16 lung

cancer samples, 16 GBM samples and 8 control samples). Through leave-one-out cross-validation, we developed regression scoring models for disease diagnosis utilizing regression models that combined the signals of protein and miRNA markers for patient classification. $***P \leq 0.001$, two-sided Student's *t* test. For lung cancer, $P = 0.0002$. For GBM, $P = 0.0002$. **f, g** ROC analyzes of the training cohort. **h, i** Assessment of the validation cohort ($n = 30$; 10 lung cancer samples, 10 GBM samples and 10 control samples). $**P \leq 0.01$, $***P \leq 0.001$, two-sided Student's *t* test. For lung cancer, $P = 0.0005$. For GBM, $P = 0.0012$. **j, k** ROC analyzes of the validation cohort. In both lung cancer and GBM, MATCH could effectively distinguish the disease samples from the healthy controls. AUC, area under the curve. All measurements were performed in triplicate ($n = 3$ independent experiments) and the data are displayed as mean \pm s.d. in (**d, e** and **h, i**) and as mean in (**b, c**). Source data are provided as a Source Data file.

leverage responsive hydrogel systems to develop a hybrid magnetic biosensor. The technology features two modular components—a versatile molecular translation module and a gradient-matched transduction module—to recognize diverse molecular targets and generate a matching magnetic response that spatially complements the sensor's intrinsic detection capability.

As compared to conventional magnetic technologies, which have limited analytical performance and require extensive sample processing, the MATCH platform is ideally suited for sensitive and direct detection of different biomolecular targets (Supplementary Table 5). First, the MATCH architecture achieves gradient-coupled transduction. MNPs are gradient-embedded within responsive hydrogel pillars and suspended over a GMR sensor array. This configuration allows the technology to tune and match multiple spatial distribution profiles, for activation, response and transduction, respectively. Specifically, the pillar microfluidics enables analyte focusing; the resultant analyte gradient achieves focal activation of the hydrogel pillars to preferentially release sensor-proximal MNPs. This triple-matched gradient architecture thus generates 3D magnetic response that spatially complements the sensor's intrinsic responsiveness. Second, the dual integration of the translation–transduction system enables programmable detection of different biomarker types. The upstream translation unit recognizes different biomarker inputs (e.g., proteins and nucleic acids) and releases universal translator sequences to activate gradient-matched transduction. Unlike conventional methods which are limited to single target detection applications (e.g., RT-qPCR for RNA detection and ELISA for protein detection), the MATCH platform demonstrates high adaptability and compatibility for cross-species comparisons among biomarkers. Furthermore, through its streamlined workflow, the integrated technology detects directly in native plasma lysates, bypasses extensive sample processing, and could be preserved through lyophilization to achieve extended stability with robust performance.

The technology has the potential to be further developed. Rational engineering of response gradients that complement the sensor's intrinsic transduction capabilities not only empowers platform development, but also expands our control to realize other applications. For example, by generating more sophisticated magnetic response gradients, through the incorporation of different nanoparticle probes^{31,32} in shape-transforming responsive systems²², the technology could be advanced to measure complex biomolecular information at a high resolution^{33,34}. Likewise, the concept could be expanded to other biosensing modalities³⁵. Through careful engineering and matching of response gradients with various transduction mechanisms (e.g., physical^{36–38} and molecular transducers^{39–41}), the approach could be exploited to enhance the performance of existing sensors and innovate integrated platforms. Finally, the modularity of the technology enables rapid assay expansion. By incorporating additional recognizer sequences⁴² in the upstream translation module, the technology could be readily extended to investigate a variety of molecular targets^{43,44}. This versatility, coupled with the platform's extended robustness through lyophilization preservation, enables the technology to be readily adapted for various biomedical applications, including multiplexed biomarker profiling^{45,46} and point-of-care clinical applications^{47,48}.

Methods

Ethical statement

This study was approved by the National University Hospital (NUH) Institutional Review Board (2016/01201, 2019/00711 and 2019/01063), National Cancer Center Singapore (NCCS) Institutional Review Board (2007/430/B) and SingHealth Centralized Institutional Review Board (SBRS2019/002). All subjects were recruited according to IRB-approved protocols after written informed consent was obtained.

GMR sensor fabrication

The GMR film, with pinned magnetization set in a selected direction, was fabricated by applying thin film deposition on a 4-inch silicon wafer (MultiDimension Technology). Using lithography and subsequent deep reactive-ion etching (Oxford Plasma), we patterned the GMR film into parallel strips. To construct the electrical pad and wire, a 5/100 nm-thick Cr/Cu layer was deposited onto the wafer by laser writing (Microtech LW405B) and thermal evaporation (Lesker Nano36). To protect the sensors and leads, a protective layer of SiO₂ (50 nm) was deposited onto the chip, excluding the pad area, through plasma-enhanced chemical vapor deposition. Finally, a Cr/Au pad was introduced by subsequent photolithography and metal deposition. Stepwise fabrication is illustrated in Supplementary Fig. 6.

DNA hydrogel patterning on GMR sensor

Hydrogel oligonucleotide sequences (Integrated DNA Technologies, IDT) can be found in Supplementary Tables 1 and 2. The pre-polymer hydrogel solution was prepared by mixing the precursor (equimolar amounts of acrydite-modified DNA crosslinker 1 and DNA crosslinker 2, and sodium acrylate monomer (Sigma)), 30-nm MNPs (Sigma) and photoinitiator I2959 (Sigma) in a phosphate-buffered saline, pH 7.4 with 10 mM MgCl₂ (PBS-Mg²⁺ buffer). Photolithography was used to pattern the hydrogel pillar array atop the GMR sensor (SUSS MJB4). Specifically, the pre-polymer solution was injected into a polydimethylsiloxane (PDMS) microfluidic channel taped on the GMR sensor and UV irradiated for 90 s under a circle-array mask. After rinsing with PBS to remove the ungelled solution, an array of pillars with pillar diameter and periodicity of 50 and 100 μm, respectively, was developed. We further optimized the effects of UV exposure time (5–90 s), precursor concentration (monomer, 5–40% w/w, with DNA crosslinkers at 100:1 molar ratio) and photoinitiator concentration (0–1.5 mg/ml) on pillar formation efficiency, defined as the percentage of pillars with < 10% size deviation from the contrast mask.

MNP encapsulation and release

To optimize the MNP encapsulation and distribution in hydrogel, we incorporated fluorescent MNPs (ATTO590-labeled MNPs, 0.5 mg/ml) as we tuned the gelation parameters. Fluorescence intensity was measured at different height of the cured hydrogel pillars as well as that of the unincorporated MNPs in supernatant to determine MNP encapsulation. With gelation parameters that achieved > 95% pillar formation efficiency (1 mg/ml photoinitiator, 10–25 s exposure time and 10–30% w/w precursor concentration), we further optimized for the highest MNP release efficiency. Specifically, MNP-encapsulated hydrogel was treated with a mixture of on-target DNA translator sequences (10 μM) and Nb.BssSI (10 units, New England Biolabs, NEB) in 1× NEBuffer r3.1 (NEB) for 20 min at room temperature. Fluorescence intensity of the released MNPs in the supernatant was measured to determine MNP release. An optimal set of gelation parameters (20 s exposure time and 20% w/w precursor with 10 mM of each DNA crosslinker) was thus determined and used for subsequent experiments. To characterize hydrogel dimension changes, the hydrogel pillars were treated with DNA translators at different concentrations (0 to 1 mM) and observed through brightfield microscopy. To characterize the morphology changes, the samples were freeze-dried in vacuum (Labconco FreeZone 4.5) and evaluated through scanning electron microscopy (FEI Verios 460) at an accelerating voltage of 2 kV.

Gradient simulation

All simulations were performed using COMSOL Multiphysics software (version 5.4). To evaluate the inherent detection capability of the GMR sensor, we first simulated the sensor's MR responsiveness to the removal of a single MNP positioned at different distance from the sensor surface (d , 0–20 μm). The physics used was Magnetic Fields, No

Currents (mfnc), where the magnetic flux density of the model MNP was fixed at 0.001 T. To investigate the effect of the GMR–hydrogel gap spacing on the MATCH signal transduction, we accounted its influence on both the MR responsiveness induced by differentially-positioned MNPs and the amount of analyte adsorption onto hydrogel pillars. For the MR responsiveness, for different GMR–hydrogel gap spacings (g , 0–15 μm), we employed the above-mentioned physics settings and simulated the response gradient using a hydrogel pillar encapsulating differentially positioned MNPs. For the analyte concentration and flow velocity profiles, we simulated them on a 3×3 array of hydrogel pillars. The physics used was Free and Porous Media Flow (fp) and Transport of Diluted Species (tds), where the porous hydrogel (porosity, 0.5; permeability, 10^{-12} m^2) was positioned in water. To evaluate the effect of gap size on analyte enrichment in the gap region, simulations were done by varying g , from 0 to 50 μm . At $0 < g < 15 \mu\text{m}$, we observed decreasing MR responsiveness and increasing analyte enrichment with larger GMR–hydrogel gap spacings. The optimal gap spacing was thus determined to maximize the overall magnetic signal by balancing both influences (see Supplementary Fig. 12 for details).

Generation and characterization of MNP gradient

To encapsulate gradient-distributed MNPs in hydrogel pillars, the optimized pre-polymer solution mixed with MNPs was first injected into a PDMS channel attached to the GMR sensor. Magnets (0.2 T, RS Components) were positioned beneath the sensor chip for 2 min, causing a MNP distribution gradient to form in the viscous pre-polymer solution. Optical lithography was subsequently applied, as previously described, to pattern the hydrogel pillars. For comparison, hydrogel pillars were similarly prepared in the absence of the magnets. To characterize the MNP gradient within hydrogel pillars, ATTO590-MNPs were used. Fluorescence images were captured at different heights of the formed pillars through confocal microscopy (Olympus Fluoview FV3000) and analyzed with ImageJ (version 1.54 g).

Generation and characterization of analyte gradient

To generate the analyte gradient, we fabricated a microfluidic channel to insert a gap between the hydrogel pillars and the sensor surface, to achieve an optimal gap spacing (g) as determined by the simulation. Stepwise fabrication of the microchannel is illustrated in Supplementary Fig. 13b. Briefly, hydrogel pillars were first prepared in a channel cavity of height h_0 constructed by applying patterned tape on a PET plastic film with a coverslip on top. On the sensor substrate, taking into account the increase in hydrogel height due to gel swelling (Δh), a PDMS layer was spin-coated (5000 rpm, 5 min) with a defined thickness (d) to generate the desired gap spacing (g). The coverslip with the formed hydrogel pillar array was then transferred to the sensor cavity. To characterize the analyte distribution adsorbed onto the formed hydrogel pillars, FAM-labeled DNA sequences were introduced and incubated for 5 min at room temperature. After washing, fluorescence images were captured at different heights of the formed pillars through confocal microscopy and analyzed with ImageJ.

Molecular translation module

Equimolar amount of target-specific biotinylated recognizer strand (10 μM) and translator strand (10 μM) (Supplementary Table 2) were pre-mixed to form the DNA molecular translation module. To immobilize the DNA recognizer, a 100 nm-thick gold pad in the MATCH microfluidic platform (chamber 1, Supplementary Fig. 6a) was immersed in a mixture of biotin–PEG–thiol (10 mM, Sigma) and methyl–PEG–thiol (10 nM, Sigma) in PBS overnight at room temperature. Following rinsing with PBS, the surface was blocked with 5% w/v bovine serum albumin (BSA, Sigma) in PBS for 1 h at room temperature. The surface was sequentially incubated with streptavidin

(0.5 mg/ml) and the recognizer–translator duplex solution for 30 min at room temperature, respectively. Following washing to remove the unbound DNA duplex, the functionalized gold pad was used for further experiments or stored at 4 $^{\circ}\text{C}$.

Translator optimization

A translator strand consists of a variable region complementary to the recognizer strand and a conserved region that hybridizes with the DNA crosslinker in the hydrogel network. To optimize the variable region, we designed FAM-labeled DNA translators by varying the length of the variable region (Supplementary Table 1). DNA recognizer–translator complexes were prepared with these translators and immobilized as previously described. After incubation with 10 μM targets for 30 min in PBS– Mg^{2+} buffer, the supernatant was collected and the resultant fluorescence intensity of the target-displaced translators was measured. To optimize the conserved region, we designed translators with different-sized conserved regions (5–21 nt). The respective translators (10 μM) were mixed with Nb.BssSI (10 units) in $1\times$ NEBuffer r3.1 and incubated with the hydrogel encapsulating ATTO590-MNPs for 20 min. The supernatant was then collected and the resultant fluorescence intensity reflective of MNP release was measured (Tecan).

MATCH microfluidic implementation

The microfluidics was fabricated using standard soft lithography. We first prepared a complementary epoxy hard mold using 3D printer (EnvisionTec). The pattern consists of three chambers (molecular translation, mixing and signal transduction modules), two inlets, one outlet and an array of parallelogram in the mixing chamber. Specifically, the signal transduction chamber was designed with a larger depth to accommodate the coverslip supporting MNP-loaded hydrogel pillars. The epoxy mold was then treated with 1% w/v trichlorosilane ethanol solution for 2 h. PDMS pre-polymer (mixing ratio 10:1) was casted onto the treated mold and heated at 75 $^{\circ}\text{C}$ for 1 h. The formed PDMS channel was treated with oxygen plasma (Harrick Plasma) to attach with the hydrogel coverslip and assembled onto the GMR chip.

Operation of the MATCH platform

Operation steps of the MATCH microfluidic chip are illustrated in Supplementary Fig. 7. A baseline GMR signal was measured prior to sample addition. Next, 1 μl sample solution was introduced through inlet 1 and incubated with the DNA recognizer complex for 30 min to enable target recognition. Valve 1 was then opened to allow the solution containing target-displaced translator stands (from the target translation module) and 1 μl enzyme solution (10 units Nb.BssSI in $2\times$ NEBuffer r3.1) (from inlet 2) to be pumped forward to mix thoroughly in the mixing module. The mixture was then introduced to the signal transduction module where it incubated with the MNP-loaded hydrogel architectures for 20 min. Finally, the released MNPs were removed through flushing with PBS– Mg^{2+} buffer and a corresponding GMR signal was registered upon the MNP removal. All fluidic flows were actuated by a syringe pump (Harvard Instruments) at a constant flow rate of 1 $\mu\text{l}/\text{min}$.

MATCH signal analysis

For all GMR measurements, a Helmholtz coil (CH-Magnetolectricity Technology) was used to generate a direct current magnetic field parallel to the GMR sensor layer. The voltage outputs were measured using a 2450 SourceMeter (Keithley Instruments). We defined the MATCH signal as follows.

$$\tilde{V} = V_{\text{after}} - V_{\text{before}} \quad (1)$$

where \tilde{V} indicates the GMR signal arising from sample incubation; V_{after} is the signal output after sample incubation; V_{before} is the baseline

signal output before sample incubation.

$$\text{MATCH signal} = \tilde{V}_{\text{target}} - \tilde{V}_{\text{control}} \quad (2)$$

where $\tilde{V}_{\text{target}}$ refers to the GMR signal associated with a recognizer for a specific target of interest, and $\tilde{V}_{\text{control}}$ refers to the signal of a sample-matched control (i.e., sample incubated with a scrambled recognizer).

Comparison of magnetic assays

To evaluate the sensitivity of the triple-matched, partially matched and unmatched configurations, we performed titration analyzes. Target DNA sequences were titrated (1 aM to 1 mM) and incubated with different sensor configurations for GMR measurements. To characterize the MNP release kinetics, we performed real-time magnetic and fluorescence measurements. Specifically, hydrogel pillars were assembled in a microfluidic channel and prepared with fluorescent ATTO590-MNPs embedded in different spatial distributions (gradient or uniform). Upon target introduction, magnetic measurements were performed directly with a GMR sensor beneath the hydrogel system, and fluorescence measurements were performed on the reaction supernatant with a plate reader (Tecan).

Lyophilization of MATCH chips

To facilitate the clinical implementation of the MATCH platform, integrated chips containing the molecular translation module and the GMR transduction module patterned with hydrogel pillars were lyophilized overnight in PBS-Mg²⁺ buffer. The stability of the lyophilized chips was evaluated after storage for up to 3 weeks at 25 °C. Specifically, the chips were first rehydrated in PBS-Mg²⁺ buffer for 10 min, before being treated with target (10 μM) and Nb.BssSI enzyme (10 units). Hydrogel dimension changes (e.g., height and diameter changes) were evaluated before and after MNP release to characterize the rehydration effect. GMR signals were acquired as described above to determine the analytical performance. To further evaluate the stiffness of the hydrogel, rheological properties of the as-fabricated DNA hydrogel and the recovered hydrogel (rehydrated after storage for 2 weeks at 25 °C) were characterized (Anton Paar MCR-302). A time sweep test was carried out at a fixed strain of 1% and frequency of 1 Hz at 25 °C for 5 min.

Comparison against conventional magnetic capture assay

To implement conventional magnetic sandwich assays, we functionalized the GMR SiO₂ surface to immobilize different capture probes (DNA for nucleic acid target or antibody for protein target). The surface was treated in 5% v/v (3-aminopropyl)triethoxysilane (APTES in ethanol, Sigma) for 15 min, rinsed and heated at 100 °C for 1 h. For DNA probe immobilization, the surface was activated with carbodiimide/N-hydroxysuccinimide chemistry (Thermo Scientific) and coupled with carboxyl-modified capture DNA probes (10 μM, Tsingke Biotech, Supplementary Table 2) at room temperature for 2 h. After washing, the functionalized sensor was incubated with target nucleic acid in a buffer of 50 mM NaCl, 1.5 mM MgCl₂, 0.1 M KCl and 50 mM Tris-HCl (pH 8.5) for 1 h at room temperature. The target-captured sensor was then treated sequentially with biotinylated detection probe (10 μM) and streptavidin-modified MNPs (0.1 μg/μl, Spherotech) to construct magnetic sandwich assemblies. After rinsing to remove unbound MNPs, GMR signals were measured via the embedded sensor. For capture antibody immobilization, the APTES-modified SiO₂ surface was incubated with 5% w/v glutaraldehyde (Sigma) at room temperature for 5 h. After blocking with 1% w/v BSA for 1 h, the surface was treated with capture antibodies (5 μg/ml, Supplementary Table 3) overnight at 4 °C. After washing, the functionalized sensor was incubated with target protein in PBS with 0.5% w/v BSA for 1 h at 37 °C. The target-captured sensor was then treated sequentially with biotinylated detection antibodies (1 μg/ml) and streptavidin-modified MNPs (0.1 μg/μl). After

rinsing to remove unbound MNPs, GMR signals were measured as previously described.

Cell culture and lysis

Human cancer cell lines were obtained from the American Type Culture Collection (ATCC) or the Center for Systems Biology at Massachusetts General Hospital (MGH). CaOV3 (ATCC, catalog no. HTB-75), DLD-1 (ATCC, catalog no. CCL-221) and HCT116 (ATCC, catalog no. CCL-247) were cultured in DMEM (HyClone) supplemented with 10% v/v fetal bovine serum (FBS, Gibco) and 1% v/v penicillin-streptomycin (Gibco). MKN45 (MGH), SNU484 (MGH), H3255 (ATCC, catalog no. CRL-2882) and PC9 (MGH) were grown in RPMI-1640 (HyClone) supplemented with 10% v/v FBS and 1% v/v penicillin-streptomycin. All cell lines were tested free of mycoplasma contamination (MycopAlert Mycoplasma Detection Kit, Lonza, LT07-418). To evaluate the assay performance in biological samples, we prepared cell lysates through different protocols and spiked in synthetic targets, before performing the MATCH measurements. Specifically, we lysed cell pellets through heating or chemical lysis. For heat treatment, cell pellets were resuspended in PBS-Mg²⁺ buffer and heated at 56 °C for 30 min, 70 °C for 5 min, 90 °C for 5 min or 80 °C before ultrasonication for 5 min (Elma). For chemical lysis, cell pellets were lysed in PBS-Mg²⁺ buffer containing varying amounts of Triton X-100 (Sigma-Aldrich) and sodium dodecyl sulfate (Sigma-Aldrich).

EV sample preparation

Cells were grown in a vesicle-depleted medium (i.e., 5% v/v vesicle-depleted FBS) for 48 h before vesicle isolation. All media containing EVs were filtered through a 0.8 μm membrane filter (Millipore), and treated by differential centrifugation (first at 10,000 g and subsequently at 100,000 g). For independent quantification of EV concentration, we used the nanoparticle tracking analysis (NTA) system (NS300, NTA v3.3, Nanosight). To achieve optimal counting, EV concentrations were adjusted to obtain ~50 vesicles in the field of view. All NTA measurements were performed with identical settings for consistency. For MATCH measurements of proteins and nucleic acids, EV samples were lysed in 1% v/v Triton X-100.

Enzyme-linked immunosorbent assay

Cell/EV lysates were adsorbed onto ELISA plates (Thermo Scientific) and blocked using 1% w/v BSA in PBS before incubation with samples. After washing with PBST, biotinylated antibodies (1 μg/ml, Supplementary Table 3) were added in PBS with 1% w/v BSA and incubated for 2 h at room temperature. Following incubation with horseradish peroxidase-conjugated streptavidin (Thermo Scientific), chemiluminescence intensity was determined using a plate reader (Tecan).

RT-qPCR quantification of RNA

RNA was extracted from cell/EV lysates with a commercial kit (miR-Neasy, Qiagen) and reverse-transcribed to generate first-strand cDNA (TaqMan MicroRNA Reverse Transcription Kit, Applied Biosystems). cDNA was pre-amplified when necessary (TaqMan PreAmp Master Mix, Applied Biosystems) before qPCR. All qPCR reactions were carried out using TaqMan Fast Advanced Master Mix (Applied Biosystems) per manufacturer's protocols, on a QuantStudio 5 Real-Time PCR System (Applied Biosystems). Amplification conditions consisted of 1 cycle of 20 °C for 2 min and 95 °C for 2 min, 45 cycles of 95 °C for 1 s and 60 °C for 20 s. All experiments were performed in triplicate. The threshold cycle (C_T) was defined as the fractional cycle number at which the fluorescence passes the fixed threshold.

Clinical samples

All specimens were obtained with informed consent from the National University Hospital (NUH) Institutional Review Board (2016/01201,

2019/00711 and 2019/01063), National Cancer Center Singapore (NCCS) Institutional Review Board (2007/430/B) and SingHealth Centralized Institutional Review Board (SBRSA2019/002). A total of 70 blood samples (26 lung cancer samples, 26 GBM samples and 18 healthy controls) were evaluated in this study. Cancer diagnoses were established from gold-standard pathology reports. For plasma collection, venous blood (5 ml) was drawn from subjects in EDTA tubes and processed immediately. Briefly, all blood samples were centrifuged for 10 min at 400 g (4 °C). Plasma was transferred without disturbing the buffy coat and centrifuged again for 10 min at 1100 g (4 °C). All plasma samples were de-identified and stored at -80 °C before MATCH measurements.

MATCH clinical measurement

For clinical analysis, plasma samples were lysed by adding 1% v/v Triton X-100 and incubating for 30 min. A 1 µl lysate sample was injected into the MATCH microfluidic chip through inlet 1 and measurements were performed as previously described. Patient sample-matched control (scrambled recognizer) was included to account for non-specific sample binding. Measurements were performed blinded from clinical diagnoses.

Statistics & reproducibility

All measurements were performed in triplicate, and the data are displayed as mean ± standard deviation. Significance tests were carried out with a two-tailed Student's *t*-test or ANOVA. For inter-sample comparisons, multiple pairs of samples were tested, and the resulting *P* values were adjusted for multiple hypothesis testing using Bonferroni correction. Values that had an adjusted *P* < 0.05 were determined as significant. Correlation analyzes were performed with Pearson's *r* to determine the goodness of fit in linear regressions. Plasma samples were randomized into two representative cohorts. Using the training patient cohort, through leave-one-out cross-validation, we developed regression scoring models for disease diagnosis with different combinations of biomarkers: protein only, miRNA only and a combination of protein and miRNA markers. The markers were selected by excluding those with *P* value > 0.1 in a linear regression model using the full marker panel. The training regression models were then applied to a validation patient cohort for independent assessment. To evaluate the clinical performance, we performed ROC curve analysis and computed the values of AUC using the trapezoidal rule. Sensitivity and specificity were calculated using standard formulas. For clinical analysis of lung cancer and GBM diagnosis, sample sizes were restricted by the availability of patient samples. No data were excluded from the analyzes. All experiments were performed blinded from the clinical diagnoses. Statistical analyzes were performed using R (version 4.2.1) and GraphPad Prism (version 9.3) software.

Reporting summary

Further information on research design is available in the Nature Portfolio Reporting Summary linked to this article.

Data availability

The main data supporting the results in this study are available within the paper and its Supplementary Information. Source data are provided with this paper.

References

- Lee, H., Shin, T. H., Cheon, J. & Weissleder, R. Recent developments in magnetic diagnostic systems. *Chem. Rev.* **115**, 10690–10724 (2015).
- Lin, G., Makarov, D. & Schmidt, O. G. Magnetic sensing platform technologies for biomedical applications. *Lab Chip* **17**, 1884–1912 (2017).
- Gaster, R. S. et al. Matrix-insensitive protein assays push the limits of biosensors in medicine. *Nat. Med.* **15**, 1327–1332 (2009).
- Marchiori, E. et al. Nanoscale magnetic field imaging for 2D materials. *Nat. Rev. Phys.* **4**, 49–60 (2022).
- Shapiro, M. G. et al. Directed evolution of a magnetic resonance imaging contrast agent for noninvasive imaging of dopamine. *Nat. Biotechnol.* **28**, 264–270 (2010).
- Cai, K. et al. Magnetic resonance imaging of glutamate. *Nat. Med.* **18**, 302–306 (2012).
- Reddy, L. H., Arias, J. L., Nicolas, J. & Couvreur, P. Magnetic nanoparticles: design and characterization, toxicity and biocompatibility, pharmaceutical and biomedical applications. *Chem. Rev.* **112**, 5818–5878 (2012).
- Gao, Y. et al. Multiplex measurement of twelve tumor markers using a GMR multi-biomarker immunoassay biosensor. *Biosens. Bioelectron.* **123**, 204–210 (2019).
- Gaster, R. S. et al. Quantification of protein interactions and solution transport using high-density GMR sensor arrays. *Nat. Nanotechnol.* **6**, 314–320 (2011).
- Gloag, L., Mehdipour, M., Chen, D., Tilley, R. D. & Gooding, J. J. Advances in the application of magnetic nanoparticles for sensing. *Adv. Mater.* **31**, 1904385 (2019).
- Issadore, D. et al. Magnetic sensing technology for molecular analyses. *Lab Chip* **14**, 2385–2397 (2014).
- Becker, C. et al. A new dimension for magnetosensitive e-skins: active matrix integrated micro-origami sensor arrays. *Nat. Commun.* **13**, 2121 (2022).
- Ha, M. et al. Printable and stretchable giant magnetoresistive sensors for highly compliant and skin-conformal electronics. *Adv. Mater.* **33**, 2005521 (2021).
- Huang, B. et al. Emergent phenomena and proximity effects in two-dimensional magnets and heterostructures. *Nat. Mater.* **19**, 1276–1289 (2020).
- Gibertini, M., Koperski, M., Morpurgo, A. F. & Novoselov, K. S. Magnetic 2D materials and heterostructures. *Nat. Nanotechnol.* **14**, 408–419 (2019).
- Haun, J. B., Devaraj, N. K., Hilderbrand, S. A., Lee, H. & Weissleder, R. Bioorthogonal chemistry amplifies nanoparticle binding and enhances the sensitivity of cell detection. *Nat. Nanotechnol.* **5**, 660–665 (2010).
- Ge, J. et al. A bimodal soft electronic skin for tactile and touchless interaction in real time. *Nat. Commun.* **10**, 4405 (2019).
- Wang, Z. et al. Dual-selective magnetic analysis of extracellular vesicle glycans. *Matter* **2**, 150–166 (2020).
- Zhong, R. et al. Hydrogels for RNA delivery. *Nat. Mater.* **22**, 818–831 (2023).
- Ulijn, R. V. et al. Bioresponsive hydrogels. *Mater. Today* **10**, 40–48 (2007).
- Zhang, L. et al. Multifunctional quantum dot DNA hydrogels. *Nat. Commun.* **8**, 381 (2017).
- Zhao, H. et al. A hydrogel-based mechanical metamaterial for the interferometric profiling of extracellular vesicles in patient samples. *Nat. Biomed. Eng.* **7**, 135–148 (2023).
- Ge, T. J. et al. A magnetic hydrogel for the efficient retrieval of kidney stone fragments during ureteroscopy. *Nat. Commun.* **14**, 3711 (2023).
- Park, J. et al. Soft, smart contact lenses with integrations of wireless circuits, glucose sensors, and displays. *Sci. Adv.* **4**, eaap9841 (2018).
- O'Brien, K., Breyne, K., Ughetto, S., Laurent, L. C. & Breakefield, X. O. RNA delivery by extracellular vesicles in mammalian cells and its applications. *Nat. Rev. Mol. Cell Biol.* **21**, 585–606 (2020).
- Shao, H. et al. Protein typing of circulating microvesicles allows real-time monitoring of glioblastoma therapy. *Nat. Med.* **18**, 1835–1840 (2012).

27. Verweij, F. J. et al. The power of imaging to understand extracellular vesicle biology in vivo. *Nat. Methods* **18**, 1013–1026 (2021).
28. Sandfeld-Paulsen, B. et al. Exosomal proteins as prognostic biomarkers in non-small cell lung cancer. *Mol. Oncol.* **10**, 1595–1602 (2016).
29. Wu, K. L., Tsai, Y. M., Lien, C. T., Kuo, P. L. & Hung, A. J. The roles of microRNA in lung cancer. *Int. J. Mol. Sci.* **20**, 1611 (2019).
30. Huang, S. W., Ali, N. D., Zhong, L. & Shi, J. MicroRNAs as biomarkers for human glioblastoma: progress and potential. *Acta Pharm. Sin.* **39**, 1405–1413 (2018).
31. Dong, L. et al. Highly hydrated paramagnetic amorphous calcium carbonate nanoclusters as an MRI contrast agent. *Nat. Commun.* **13**, 5088 (2022).
32. Ananta, J. S. et al. Geometrical confinement of gadolinium-based contrast agents in nanoporous particles enhances T1 contrast. *Nat. Nanotechnol.* **5**, 815–821 (2010).
33. Sundah, N. R. et al. Barcoded DNA nanostructures for the multiplexed profiling of subcellular protein distribution. *Nat. Biomed. Eng.* **3**, 684–694 (2019).
34. Kamath, T. et al. Single-cell genomic profiling of human dopamine neurons identifies a population that selectively degenerates in Parkinson's disease. *Nat. Neurosci.* **25**, 588–595 (2022).
35. Natalia, A., Zhang, L., Sundah, N. R., Zhang, Y. & Shao, H. Analytical device miniaturization for the detection of circulating biomarkers. *Nat. Rev. Bioeng.* **1**, 481–498 (2023).
36. Yesilkoy, F. et al. Ultrasensitive hyperspectral imaging and biodection enabled by dielectric metasurfaces. *Nat. Photon* **13**, 390–396 (2019).
37. Pan, S. et al. Extracellular vesicle drug occupancy enables real-time monitoring of targeted cancer therapy. *Nat. Nanotechnol.* **16**, 734–742 (2021).
38. Rodríguez-Lorenzo, L., de la Rica, R., Álvarez-Puebla, R. A., Liz-Marzán, L. M. & Stevens, M. M. Plasmonic nanosensors with inverse sensitivity by means of enzyme-guided crystal growth. *Nat. Mater.* **11**, 604–607 (2012).
39. Hao, L. et al. CRISPR-Cas-amplified urinary biomarkers for multiplexed and portable cancer diagnostics. *Nat. Nanotechnol.* **18**, 798–807 (2023).
40. Chen, Y. et al. Collaborative equilibrium coupling of catalytic DNA nanostructures enables programmable detection of SARS-CoV-2. *Adv. Sci.* **8**, e2101155 (2021).
41. Zhang, Y. et al. Multiplexed RNA profiling by regenerative catalysis enables blood-based subtyping of brain tumors. *Nat. Commun.* **14**, 4278 (2023).
42. You, M. et al. DNA probes for monitoring dynamic and transient molecular encounters on live cell membranes. *Nat. Nanotechnol.* **12**, 453–459 (2017).
43. Hansson, O. Biomarkers for neurodegenerative diseases. *Nat. Med.* **27**, 954–963 (2021).
44. Broto, M. et al. Nanozyme-catalysed CRISPR assay for preamplification-free detection of non-coding RNAs. *Nat. Nanotechnol.* **17**, 1120–1126 (2022).
45. Yin, F. et al. DNA-framework-based multidimensional molecular classifiers for cancer diagnosis. *Nat. Nanotechnol.* **18**, 677–686 (2023).
46. Yelleswarapu, V. et al. Mobile platform for rapid sub-picogram-per-milliliter, multiplexed, digital droplet detection of proteins. *Proc. Natl Acad. Sci. USA* **116**, 4489–4495 (2019).
47. Yeh, E. C. et al. Self-powered integrated microfluidic point-of-care low-cost enabling (SIMPLE) chip. *Sci. Adv.* **3**, e1501645 (2017).
48. Zhao, H. et al. Accessible detection of SARS-CoV-2 through molecular nanostructures and automated microfluidics. *Biosens. Bioelectron.* **194**, 113629 (2021).

Acknowledgements

The authors thank the clinical team members from the National University Hospital, Singapore, National Cancer Center Singapore, Singapore and National Neuroscience Institute, Singapore, for patient sample collection, and Olivia Seow for critically proofreading the manuscript. The authors acknowledge the facilities, and the scientific and technical assistance of the Confocal Microscopy Laboratory at Center for Bioimaging Sciences, Department of Biological Sciences, National University of Singapore. This work was supported in part by funding from National University of Singapore (NUS), NUS Research Scholarship and Institute for Health Innovation & Technology. H.S. discloses support for the research from Ministry of Education [T2EP30123-0031], National Medical Research Council [OFIRG23jul-0066, MOH-000564, MOH-000541] and National Research Foundation, Singapore [NRF-CRP29-2022-0001].

Author contributions

Y.C., L.Z., and H.S. designed the research. Y.C., L.Z., X.W., X.S., N.R.S., C.Y.W., and A.N. performed the research. J.K.C.T., D.W.L., B.C., B.T.A., C.T., and T.P.L. provided de-identified clinical samples and health information. B.T.A. and C.T. established the banked resource of de-identified patient GBM tumors and associated biofluids. Y.C., L.Z., X.W., X.S., N.R.S., C.Y.W., A.N., and H.S. analyzed the data and wrote the manuscript. X.W. and X.S. contributed equally. All authors contributed to the manuscript.

Competing interests

The authors declare no competing interests.

Additional information

Supplementary information The online version contains supplementary material available at <https://doi.org/10.1038/s41467-024-52754-z>.

Correspondence and requests for materials should be addressed to Huilin Shao.

Peer review information *Nature Communications* thanks the anonymous, reviewer(s) for their contribution to the peer review of this work. A peer review file is available.

Reprints and permissions information is available at <http://www.nature.com/reprints>

Publisher's note Springer Nature remains neutral with regard to jurisdictional claims in published maps and institutional affiliations.

Open Access This article is licensed under a Creative Commons Attribution-NonCommercial-NoDerivatives 4.0 International License, which permits any non-commercial use, sharing, distribution and reproduction in any medium or format, as long as you give appropriate credit to the original author(s) and the source, provide a link to the Creative Commons licence, and indicate if you modified the licensed material. You do not have permission under this licence to share adapted material derived from this article or parts of it. The images or other third party material in this article are included in the article's Creative Commons licence, unless indicated otherwise in a credit line to the material. If material is not included in the article's Creative Commons licence and your intended use is not permitted by statutory regulation or exceeds the permitted use, you will need to obtain permission directly from the copyright holder. To view a copy of this licence, visit <http://creativecommons.org/licenses/by-nc-nd/4.0/>.

© The Author(s) 2024

¹Institute for Health Innovation & Technology, National University of Singapore, Singapore, Singapore. ²Department of Biomedical Engineering, College of Design and Engineering, National University of Singapore, Singapore, Singapore. ³Department of Medicine, Yong Loo Lin School of Medicine, National University of Singapore, Singapore, Singapore. ⁴Department of Surgery, Yong Loo Lin School of Medicine, National University of Singapore, Singapore, Singapore. ⁵Division of Medical Oncology, National Cancer Centre Singapore, Singapore, Singapore. ⁶Institute of Molecular and Cell Biology, Agency for Science, Technology and Research, Singapore, Singapore. ⁷Centre for Clinician-Scientist Development, Duke-NUS Medical School, Singapore, Singapore. ⁸Clinical Pharmacology Laboratory, National Cancer Centre Singapore, Singapore, Singapore. ⁹Singapore Immunology Network, Agency for Science, Technology and Research, Singapore, Singapore. ¹⁰National Neuroscience Institute, Singapore, Singapore. ¹¹Duke-NUS Medical School, Singapore, Singapore. ¹²SG Enable, Innovation, Singapore, Singapore. ¹³Department of Laboratory Medicine, National University Hospital, Singapore, Singapore. ¹⁴These authors contributed equally: Yuan Chen, Li Zhang. ✉ e-mail: huilin.shao@nus.edu.sg